# Optimal Advance Angle for Aided Maximum-Speed-Node Design of Switched Reluctance Machines

Roberto Rocca, *Student Member, IEEE,* Fabio Giulii Capponi, *Member, IEEE*, Savvas Papadopoulos, *Member, IEEE*, Giulio De Donato, *Senior Member, IEEE*, Mohamed Rashed, *Member, IEEE*, and Michael Galea, *Senior Member, IEEE*

*Abstract*-- **In the design processes of Switched Reluctance Machines that operate in wide constant power speed ranges, the maximum power available at maximum speed must be evaluated for every machine candidate. This is critical to ensure compliance with the power requirement. Important parameters to include in the design routine are the duration of the energizing period and the advance of the turn-on instant, i.e. advance angle. The latter is highly related to the machine geometry and is usually evaluated through time-consuming finite-element-based iterative methods. In this paper, a simple, yet novel analytical model is proposed to cater for the torque-maximising advance angle in a closed-form analytical expression, directly from the machine geometry. The goal is to provide a non-iterative design tool that speeds up the design process. Successful validations against finite element analyses and experimental results on an SR machine prototype are reported. The main outcome of this paper is shown by the improvement in computation time, without any significant loss of accuracy.**

*Index Terms*-- **Analytical Model, Advance Angle, Design Optimization, Machine Design, High Speed, Single-Pulse Mode, Switched Reluctance Machine, Torque Maximization.**

## I. INTRODUCTION

THE Switched Reluctance (SR) machine is nowadays considered a viable candidate for several engineering
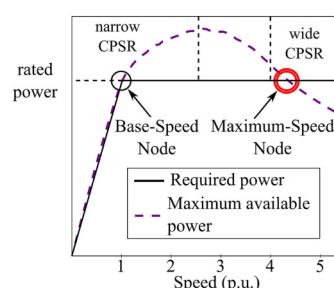
Fig. 1. Typical required power vs. speed envelope (black) and maximum power vs. speed locus (purple dashed).

applications, thanks to its rugged, robust and permanent-magnet-free rotor structure [1-5], as well as its suitability for harsh environments, [6], and its capability of covering wide Constant Power Speed Ranges (CPSR), [7], [8].

A typical power vs. speed curve of an application that requires a constant power operation is shown in Fig. 1. The demanded power increases linearly until the base-speed node and then remains constant until the maximum-speed node. In Fig. 1, the dashed curve shows a typical trend of the maximum power for an SR machine. When a design for wide CPSR is required, i.e. the ratio between maximum speed and base speed is 3.5:1 or higher, the maximum available power rapidly decreases as the speed increases, since the high pseudo back-emf prevents the fast rising of the torque-producing current, [9].

Traditionally, in order to meet this requirement, an iterative, two-node design methodology is needed, [1], [3]. The machine performance is evaluated one node at a time and the design is iterated until convergence is achieved. For the base-speed node, design techniques are well-established, such as heuristic methods, [10], [11], optimization algorithms, [4], [12], etc., even though a novel, design-space based approach has been recently proposed, [13]. For the maximum-speed node, designers focus mostly on the rotor shape improvement, [1], [2], as well as on advanced control strategies, [5], being the main objective to satisfy the rated power requirement.

To ensure compliance with the power requirement of each design candidate, the maximum torque at the maximum speed node must be evaluated. This last is usually computed through a set of Finite Element Analysis (FEA)

simulations and, since such a task is required for every machine candidate, this process may considerably increase the overall design computation time.

At maximum speed, operation in single-pulse mode must be considered, [14]. For a given machine geometry, the output torque depends on three parameters, namely the dc-bus voltage, the duration of the energizing period (dwell period) and the advance angle. It is widely known that most of the applications that require a wide CPSR, e.g. automotive and aerospace, have a limited dc-bus voltage. Therefore, it is critical to evaluate the dwell period and the advance angle that provide the maximum torque. Then, at a later design stage, the control angles may be further refined to address also other design targets, such as the efficiency. In this case, a much lower sensitivity to the control angles compared to the torque is expected, [15], [16].

It has been widely proven that the maximum torque in single-pulse mode is achieved with a dwell period equal to 180° (elec.), [17-22]. For the sake of completeness, this assumption is verified in Section II. On the other hand, various torque-maximising advance angles can be found across the literature, e.g. 128° (elec.) in [21], 80° (elec.) in [18], or 79° (elec.) in [22]. Such differences are due to the strict relationship between the torque-maximising advance angle and the machine geometry, which has traditionally forced designers to evaluate the torque-maximising advance angle with FEA-based iterative optimisation algorithms, e.g. the simplex method, [18], or search-grids, [22]. Even though these algorithms guarantee high levels of accuracy, they are highly time-consuming and require considerable implementation efforts.

Therefore, the aim of this paper is to propose an analytical model that identifies the torque-maximising advance angle in a closed-form expression, directly from the machine geometry. On the other hand, in order to achieve such a closed-form expression, the model neglects resistive voltage drop and magnetic saturation effects. Consequently, once the torque-maximising advance angle is found, an FEA simulation is still required to compute the actual value of the maximum torque with adequate accuracy. In any case, only a one-shot FEA simulation is now sufficient. As a result, the maximum torque determination becomes very fast and straightforward. Any need for iterative algorithms to evaluate the torque-maximising advance angle is removed and the two-node design process is dramatically sped up, without any significant loss of accuracy.

The proposed model is developed in Section III. The closed-form expression of the torque-maximising advance angle is given in Section IV and validated against FEA and experimental results in Section V. Finally, in Section VI, a deeper insight into the design at the maximum-speed node is given.

## II. DESIGN CONSIDERATIONS FOR THE MAXIMUM-SPEED NODE OF A WIDE-CPSR SR MACHINE

This Section provides some brief considerations concerned with the design at the maximum-speed node of high-speed, wide-CPSR SR machines.

The SR machine is typically energized by a unidirectional asymmetric H-bridge, Voltage Source Inverter (VSI), [23]. When the phase voltage $v_{ph}$ is applied to one phase, the terminal voltage equation can be expressed by (1), [1], where $i_{ph}$ is the phase current, $\omega$ is the angular speed and $R$ and $L$ are the phase resistance and inductance. The first two terms in (1) represent the resistive and inductive voltage drops. The third term is known as the machine pseudo back-emf.

$$v_{ph} = Ri_{ph} + L(\theta, i_{ph})\frac{di_{ph}}{dt} + i_{ph}\frac{\partial L(\theta, i_{ph})}{\partial \theta}\omega \qquad (1)$$

At high speeds, $\omega$ is sufficiently high for the 'pseudo' back-emf to dominate over the other voltage drops, which becomes comparable to the phase voltage, as shown in (2).

$$i_{ph}\frac{\partial L(\theta, i_{ph})}{\partial \theta}\omega \gg Ri_{ph} + L(\theta, i_{ph})\frac{di_{ph}}{dt} \qquad (2)$$

In this condition, $i_{ph}$ is limited by the pseudo back-emf itself, and any need for conditioning the phase current through the inverter, e.g. chopping, is removed. This resulting operating mode is named 'single-pulse', as each converter leg is switched on only once per cycle.

Expression (2) represents the operating conditions that typically occur at the maximum-speed node, indicating that single-pulse mode must be considered to evaluate the machine performance. The typical single-pulse phase voltage and phase current vs. the rotor position $\theta$ waveforms are illustrated in Fig. 2. In addition, the corresponding inductance vs. rotor position profile is shown. As it can be observed, single-pulse operation is defined by three control parameters, namely the dc-bus voltage $V_{DC}$, as well as two control angles. For these last, $\Theta_{dwell}$ and $\theta_{ad}$ are commonly used. $\Theta_{dwell}$ indicates the duration of the 'dwell' or 'energising' period, during which the positive $+V_{DC}$ is
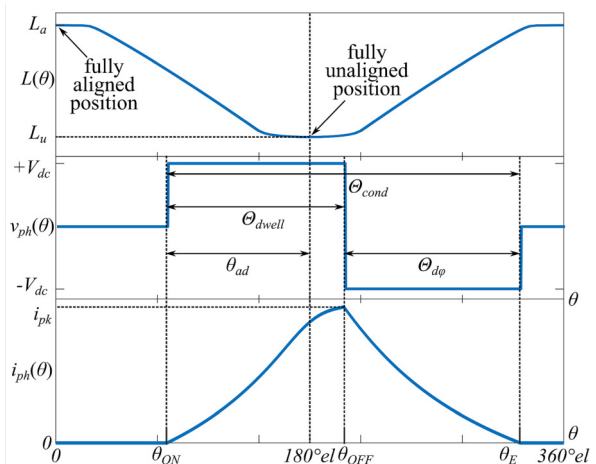


Fig. 2 Example of inductance profile and typical phase voltage and phase current waveforms in single-pulse mode.

applied across the phase winding. $\theta_{ad}$ is referred to as 'advance angle', as it indicates the advance of the turn-on position $\theta_{ON}$ with respect to the minimum point of the inductance profile (if motoring mode is assumed), [14].

For the design at the maximum-speed node, the first yet most important task is to verify that the maximum power available is at least equal to the rated power. For this purpose, the maximum $V_{DC}$ available is taken, along with the combination $\Theta_{dwell}$, $\theta_{ad}$ that caters for the maximum torque. At this point, if the power requirement is not met, the candidate at hand must be discarded. By contrast, if compliance with the power requirement is met, the design process can carry on.

The effects that $\Theta_{dwell}$ and $\theta_{ad}$ have over the average output torque $T_{avg}$ in single-pulse mode are shown in Fig. 3. The plots represent the FEA results of the prototype SR machine described in Section V. Fig. 3 shows $T_{avg}$ as a function of $\theta_{ad}$ for different $\Theta_{dwell}$. In accordance with the results provided in [17-22], the maximum output torque (solid purple line) is achieved with a dwell period of 180° (elec.). This coincides with the standard dwell period limit, since greater values might not allow the phase current to decay to zero at the end of each cycle. Fig. 3 also shows that a considerable advance angle is required to reach high torque levels at high speeds. Indeed, such an early magnetization allows the phase current to rise to a sufficiently high level before the instantaneous back-emf becomes comparable to the instantaneous phase voltage. As previously discussed, the evaluation of the torque-maximising advance angle is traditionally tackled through FEA-based optimisation processes.

A final design consideration is related to the magnetic saturation. For the operation shown in Fig. 2, Fig. 4 illustrates the corresponding $i_{ph}$ vs. phase flux linkage $\Psi_{ph}$ loop, whose subtended area represents the amount of energy that each phase converts into mechanical work in one cycle, [14]. From Fig. 4, it can be seen that even though $i_{ph}$ reaches a considerably high peak value $i_{pk}$, the highest values are reached when the inductance is around its lowest value. Consequently, $\Psi_{ph}$ remains well below the saturated region. This behaviour justifies the widely accepted assumption that saturation effects can be neglected for
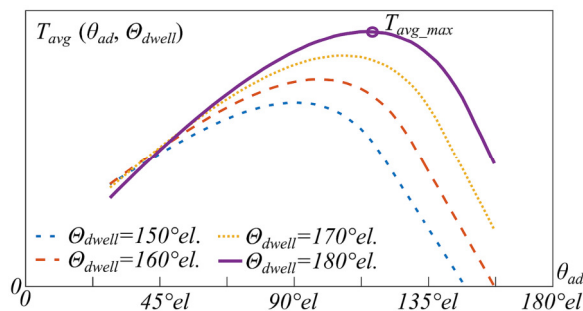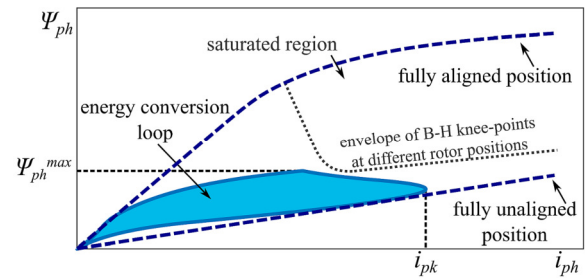


Fig. 4. SR machine operation in single-pulse mode: current vs. flux linkage energy-conversion loop.

design at the maximum-speed node of wide-CPSR SR machines, [24]. From a more general perspective, it can be noted that for progressively increasing speeds, the peak phase current tends to drop, leading to a reduction in both the resistive voltage drop and magnetic saturation effects. Hence, the more the speed, the more the two simplifying hypotheses introduced in the model are accurate.

In Section III, all the design considerations illustrated above are used to develop a 'linear' analytical model of the operating conditions at hand.

## III. LINEAR ANALYTICAL MODEL

This Section describes the analytical model that is used to express the average output torque $T_{avg}$ ($\theta_{ad}$) as a function of $\theta_{ad}$. The expression $T_{avg}$ ($\theta_{ad}$) is subsequently used in Section IV to determine the torque-maximising advance angle.

### A. Model Assumptions

The model is based on the following assumptions:
1. according to the discussion in Section II, magnetic saturation is neglected,
2. the machine operates in steady-state conditions with a constant speed of rotation $\omega$,
3. the mutual coupling between phases is negligible,
4. the resistive voltage drop is negligible,
5. an asymmetric H-bridge VSI topology is considered,
6. the machine operates in single-pulse mode,
7. the dwell period is set to 180° (elec.), in order to maximize the output torque.

### B. Initial Equations

The inductance, phase voltage and phase flux linkage are now derived with respect to the rotor position over one cycle, whose value in radians is equal to $2\pi/P_r$, where $P_r$ is the number of rotor poles.

#### 1) Inductance Profile

The initial rotor position $\theta=0$ is considered at the full alignment between one stator and one rotor tooth, as shown in Fig. 5(a). As the rotor moves, the two facing poles remain fully overlapped until the position $\theta_1$ is reached. Fig. 5(b) and Fig. 5 (c) show respectively the full-overlap condition and the position $\theta_1$. The expression for $\theta_1$ is given



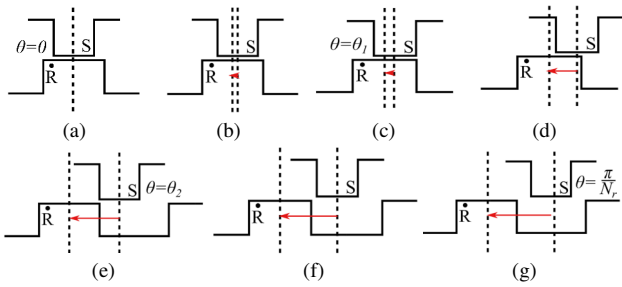Fig. 3. SR machine operation in single-pulse mode: torque vs. advance angle for different dwell periods.

Fig. 5. Inductance Profile: (a) $\theta=0$, (b) full-overlap region, (c) $\theta=\theta_1$, (d) partial-overlap region, (e) $\theta=\theta_2$, (f) non-overlap region, (g) $\theta=\pi/P_r$.

in (3), where $\beta_{st}$ and $\beta_{rt}$ are the stator and rotor pole arcs respectively. As the rotation continues, the two facing poles overlap only partially, as in Fig. 5(d). Such partial-overlap region terminates at the position $\theta_2$, which is shown in Fig. 5(e) and whose equation is given by (4). At $\theta_2$, the non-overlap region commences, which is represented in Fig. 5(f). Finally, the maximum misalignment condition occurs at $\theta=\pi/P_r$, represented in Fig. 5(g). Then, the profile symmetrically repeats.

$$\theta_1 = \frac{\beta_{rt} - \beta_{st}}{2} \tag{3}$$

$$\theta_2 = \frac{\beta_{rt} + \beta_{st}}{2} \tag{4}$$

In its most simple form, the inductance profile is described by a trapezoidal locus, where fringing and rounding phenomena are neglected, [25]. In the full-overlap region, $0 \leq \theta \leq \theta_1$, the inductance is considered constant at its maximum $L_a$, as represented in Fig. 6(a). In the partial-overlap region, $\theta_1 \leq \theta \leq \theta_2$, the profile descends linearly. Finally, in the non-overlap region, $\theta_2 \leq \theta \leq \pi/P_r$, the profile remains constantly at the minimum inductance $L_u$, as shown in Fig. 6(b).

As discussed in Section II, the highest cycle currents in single-pulse mode occur when the inductance is at its lowest, i.e. in the non-overlap region. Basing on that, the following considerations can be done:

- Due to the low current levels, the constant-inductance representation in the full-overlap region can be maintained (see Fig. 6(a));
- The linear descent in the partial overlap region may be maintained as well, as it gives a very good compromise between accuracy and simplicity of mathematical formulation;
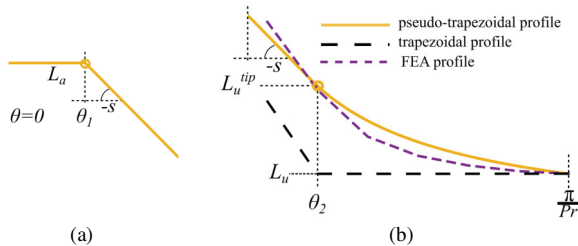- A precise modelling of the non-overlap region is

critical, due to the high current levels. A typical trend of the inductance within the non-overlap region, found via FEA, is plotted in Fig. 6(b).

As it can be noted, the inductance progressively decays to $L_u$ because of the effects of fringing and rounding phenomena. Consequently, the simple trapezoidal profile might excessively underestimate the inductance within the region. This, in turn, may cause strong inaccuracies in the calculation of the phase current as well as of the inductance derivative, resulting in a significantly inaccurate output torque. In order to avoid such an issue, this work proposes a 'pseudo-trapezoidal' inductance profile, in which the non-overlap region is modelled with a Fröhlich-like expression, [26]. The non-overlap region inductance modelled via a Fröhlich-like expression is plotted in Fig. 6(b), where a close match with the FEA locus is observed. In this way, the output torque can be more accurately estimated.

The partial-overlap and non-overlap regions of the proposed pseudo-trapezoidal profile are defined as follows. In the partial-overlap region, the inductance decays linearly, but his time until the 'tip' point ($\theta_2$, $L_u^{tip}$) is reached. The slope $s$ of the inductance in this region is given by (5). In the non-overlap region, the inductance descends from $L_u^{tip}$ to $L_u$ following the aforementioned Fröhlich-like trend, whose analytical expression is defined by $s$, $L_u$, $L_u^{tip}$ and by the coefficient $f_r$. The latter is expressed by (6).

$$s = \frac{L_a - L_u^{tip}}{\theta_2 - \theta_1} \tag{5}$$

$$f_r = \frac{\left(L_u^{tip} - L_u\right)\left(\dfrac{\pi}{P_r} - \theta_2\right)}{s\left(\dfrac{\pi}{P_r} - \theta_2\right) - \left(L_u^{tip} - L_u\right)} \tag{6}$$

The analytical expression of the entire pseudo-trapezoidal profile is given by (7), while Fig. 7 graphically illustrates it.

$$L(\theta) = \begin{cases} L_a & 0 \leq \theta \leq \theta_1 \\[2mm] L_a - s(\theta - \theta_1) & \theta_1 \leq \theta \leq \theta_2 \\[2mm] L_u^{tip} - \dfrac{sf_r(\theta - \theta_2)}{f_r + (\theta - \theta_2)} & \theta_2 \leq \theta \leq \dfrac{\pi}{P_r} \\[4mm] L_u^{tip} + \dfrac{sf_r\left(\theta + \theta_2 - \dfrac{2\pi}{P_r}\right)}{f_r - \left(\theta + \theta_2 - \dfrac{2\pi}{P_r}\right)} & \dfrac{\pi}{P_r} \leq \theta \leq \dfrac{2\pi}{P_r} - \theta_2 \\[4mm] L_a + s\left(\theta + \theta_1 - \dfrac{2\pi}{P_r}\right) & \dfrac{2\pi}{P_r} - \theta_2 \leq \theta \leq \dfrac{2\pi}{P_r} - \theta_1 \\[4mm] L_a & \dfrac{2\pi}{P_r} - \theta_1 \leq \theta \leq \dfrac{2\pi}{P_r} \end{cases} \tag{7}$$



Fig. 6. Inductance Profile: (a) Aligned region, (b) Unaligned region.

Eq. (7) highlights that $L_a$, $L_u^{tip}$ and $L_u$ are needed to determine the profile. To evaluate them, three static FEA simulations would be theoretically enough.

However, since two-node designs are usually started from the base-speed node, it is reasonable to consider the three inductances as already known parameters.

A further advantage provided by the Fröhlich-like expression can be noted in (7). In fact, the mathematical expression of the inductance within the non-overlap region, i.e. $\theta_2 \leq \theta \leq \pi/P_r$ and $\pi/P_r \leq \theta \leq 2\pi/P_r$-$\theta_2$, is strictly monotonic, which means that the decaying profile shape is preserved for any machine geometry, as no undesired shapes can arise from the interpolation process.

*2) Voltage and Flux Linkage Waveforms*

In single-pulse operating conditions, the full dc-voltage $V_{DC}$ is applied across the phase between $\theta_{ON}$ and $\theta_{OFF}$. Since the dwell period equals half the electric period, $\theta_{ON}$ and $\theta_{OFF}$ can be written as functions of $\theta_{ad}$ and $\Theta_{dwell}$, as in (8) and (9).

$$\theta_{ON} = \frac{\pi}{P_r} - \theta_{ad} \tag{8}$$

$$\theta_{OFF} = \theta_{ON} + \Theta_{dwell} = \frac{2\pi}{P_r} - \theta_{ad} \tag{9}$$

Once the off signal is triggered, the dc-voltage is reversed and since the resistive voltage drop is neglected, the de-fluxing period has the same duration as the dwell, i.e. half the electric period. The resulting phase voltage vs. rotor position characteristic is a rectangular waveform, as shown in Fig. 8. The phase-voltage expression as a function of the rotor position, for a given $\theta_{ad}$, is given in (10).

$$v_{ph}\left(\theta, \theta_{ad}\right) = \begin{cases} -V_{DC} & 0 \leq \theta \leq \dfrac{\pi}{P_r} - \theta_{ad} \\[2mm] +V_{DC} & \dfrac{\pi}{P_r} - \theta_{ad} \leq \theta \leq \dfrac{2\pi}{P_r} - \theta_{ad} \\[2mm] -V_{DC} & \dfrac{2\pi}{P_r} - \theta_{ad} \leq \theta \leq \dfrac{2\pi}{P_r} \end{cases} \tag{10}$$

For steady-state operation at constant speed, the phase flux linkage $\Psi_{ph}$ can be determined by simply integrating $v_{ph}$. To perform the integration, the boundary condition needs to express the condition of full core demagnetization at the turn-on instant, i.e. $\Psi_{ph}$ ($\pi/P_r$-$\theta_{ad}$)=0. The result is a triangular waveform, as illustrated in Fig. 9. The resulting flux linkage expression, for a given $\theta_{ad}$, is reported in (11).

$$\Psi_{ph}\left(\theta, \theta_{ad}\right) = \begin{cases} -\dfrac{V_{DC}}{\omega}\left(\theta + \theta_{ad} - \dfrac{\pi}{P_r}\right) & 0 \leq \theta \leq \dfrac{\pi}{P_r} - \theta_{ad} \\[2mm] \dfrac{V_{DC}}{\omega}\left(\theta + \theta_{ad} - \dfrac{\pi}{P_r}\right) & \dfrac{\pi}{P_r} - \theta_{ad} \leq \theta \leq \dfrac{2\pi}{P_r} - \theta_{ad} \\[2mm] -\dfrac{V_{DC}}{\omega}\left(\theta + \theta_{ad} - \dfrac{3\pi}{P_r}\right) & \dfrac{2\pi}{P_r} - \theta_{ad} \leq \theta \leq \dfrac{2\pi}{P_r} \end{cases} \tag{11}$$
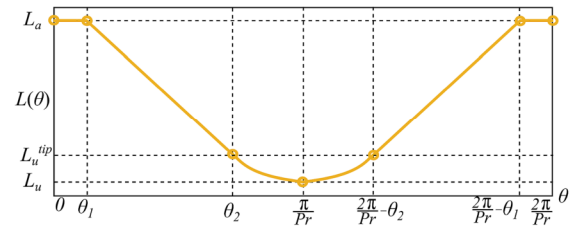


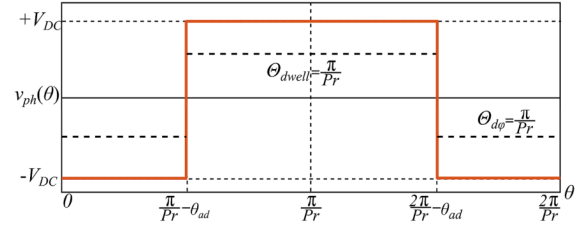Fig. 7. Pseudo-Trapezoidal Inductance Profile.



Fig. 8. Single-pulse, rectangular voltage vs. rotor position waveform in output torque maximization mode.
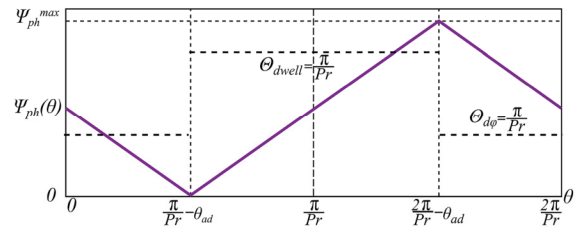


Fig. 9. Single-pulse, triangular flux linkage vs. rotor position waveform in output torque maximization mode.

### C. Phase Current, Phase Torque and Output Torque Prediction

The expression of the phase current as a function of the rotor position and a given $\theta_{ad}$, $i_{ph}(\theta, \theta_{ad})$ can be found by the ratio between the phase flux linkage and the inductance, as shown in (12). From the expression of the phase current, it is then possible to obtain the torque per phase $T_{ph}$, as in (13). The average torque produced by one phase, $T_{ph\_avg}$ ($\theta_{ad}$), is expressed by (14). Finally, since the $m$ phases are controlled with the same advance angle and dwell period, the average torque produced by each phase is the same.

$$i_{ph}\left(\theta, \theta_{ad}\right) = \frac{\Psi_{ph}\left(\theta, \theta_{ad}\right)}{L\left(\theta\right)} \tag{12}$$

$$T_{ph}\left(\theta, \theta_{ad}\right) = \frac{1}{2} i_{ph}\left(\theta, \theta_{ad}\right)^2 \frac{dL\left(\theta\right)}{d\theta} \tag{13}$$

$$T_{ph\_avg}\left(\theta_{ad}\right) = \frac{P_r}{2\pi} \int_0^{\frac{2\pi}{P_r}} T_{ph}\left(\theta, \theta_{ad}\right) d\theta \tag{14}$$

Therefore, the average overall torque for a given $\theta_{ad}$, $T_{avg}$ ($\theta_{ad}$), is equal to $m$ times $T_{ph\_avg}$ ($\theta_{ad}$), as shown in (15). This expression is used in the next Section to derive the advance angle that maximizes $T_{avg}$.

$$T_{avg}\left(\theta_{ad}\right)=mT_{ph\_avg}\left(\theta_{ad}\right)=m\frac{P_r}{2\pi}\int_0^{\frac{2\pi}{P_r}}T_{ph}\left(\theta,\theta_{ad}\right)d\theta$$

$$=m\frac{P_r}{4\pi}\int_0^{\frac{2\pi}{P_r}}i_{ph}\left(\theta,\theta_{ad}\right)^2\frac{dL(\theta)}{d\theta}d\theta$$

(15)

## IV. TORQUE-MAXIMISING ADVANCE ANGLE

The advance angle that maximises the output torque, $\theta_{ad}^*$, can be obtained from (15) by simply setting equal to zero the derivative of $T_{avg}$ $(\theta_{ad})$ with respect to $\theta_{ad}$, as shown in (16).

$$\frac{dT_{avg}(\theta_{ad})}{d\theta_{ad}}=0$$

(16)

Then, substituting (12) and the derivative of (7) with respect to $\theta$ into (15), (17) is derived.

$$\frac{dT_{ph\_avg}(\theta_{ad})}{d\theta_{ad}}=m\frac{P_r}{2\pi}\frac{V_{DC}^2}{\omega^2}\left[\frac{B\theta_{ad}+C}{D\theta_{ad}+E}+F\right]=0$$

(17)

Terms B, C, D, E and F are expressed respectively by (19), (20), (21), (22) and (23). $\theta_{ad}^*$ is finally obtained by (18). Considering B, C, D, E and F, it is observed that the torque-maximising angle is independent of $V_{DC}$ and $\omega$. In other words, $\theta_{ad}^*$ is only a function of the parameters that define the inductance vs. rotor position profile, i.e. the machine geometry and number of turns. This fact remarks the importance of a precise modelling of the inductance profile.

$$\theta_{ad}^*=-\frac{FE+C}{B+FD}$$

(18)

Once the advance angle $\theta_{ad}^*$ is found, a single-shot FEA is sufficient to identify the maximum torque. In this way, the nonlinear behaviour of the magnetic material can be taken back into account and accuracy for the maximum torque estimation can be maintained.

## V. FEA AND EXPERIMENTAL VALIDATION

In this Section, a 12/8 SR machine is used to validate the analytical model developed in Section III and hence confirm the validity of the closed-form expression of $\theta_{ad}^*$ given in (23). The validation is carried out in two steps: 1) comparison of the analytical inductance profile versus the FEA and experimental values, and 2) comparison of the torque vs. advance angle for different speeds and voltages.

A FEA model of the machine is built. A physical prototype is manufactured and set up on a high-speed rig. Consistently with the assumptions made in Section III, the FEA has been built by using an ideal iron with a $10^6$ H/m permeability. Fig. 10(a) shows the 2D geometry of the FEA model, while Fig. 10(b) a cross-sectional view of the physical prototype. Machine specifications are given in Table I.

TABLE I
Geometry and nameplates ratings of the modelled and tested SRM

| Parameter | Measure Unit | Value |
|---|---|---|
| Rated Peak Voltage | V | 36 |
| Rated RMS Current | A | 26 |
| Maximum Speed | rpm | 6000 |
| Stator Poles | - | 12 |
| Rotor Poles | - | 8 |
| Outer Diameter | mm | 137.8 |
| Stator Tooth Angle | ° | 15.2 |
| Rotor Tooth Angle | ° | 17.1 |
| Axial Stack Length | mm | 80 |

$$B=-4\left(L_a-L_u^{tip}\right)\left[L_a^2\left(\frac{\pi}{P_r}-\theta_2\right)-L_u^{tip2}\theta_1-L_aL_u^{tip}\left(\frac{\pi}{P_r}-\theta_1\left(1-\ln\left(\frac{L_a}{L_u^{tip}}\right)\right)-\theta_2\left(1+\ln\left(\frac{L_a}{L_u^{tip}}\right)\right)\right)\right]$$

(19)

$$C=\begin{aligned}&2\left[\left(L_a-L_u^{tip}\right)\left(L_u^{tip}\theta_1\left(L_a\theta_2-L_u^{tip}\theta_1+\frac{\pi}{P_r}\left(L_a-L_u^{tip}\right)\right)-L_a\theta_2\left(L_a\theta_2-L_u^{tip}\theta_1-\frac{\pi}{P_r}\left(L_a-L_u^{tip}\right)\right)\right)\right]+\\&+2\left[L_aL_u^{tip}\left(L_a\theta_2-L_u^{tip}\theta_1\right)\left(2\ln\left(\frac{L_a}{L_u^{tip}}\right)\left(\theta_2-\theta_1\right)+\left(\frac{1}{L_a}-\frac{1}{L_u^{tip}}\right)\left(L_a\theta_2-L_u^{tip}\theta_1-\frac{\pi}{P_r}\left(L_a-L_u^{tip}\right)\right)\right)\right]\end{aligned}$$

(20)

$$D=-L_aL_u^{tip}P_r\left(L_a-L_u^{tip}\right)\left(\theta_2-\theta_1\right)$$

(21)
$$E=L_aL_u^{tip}P_r\left(L_a\theta_2-L_u^{tip}\theta_1\right)\left(\theta_2-\theta_1\right)$$

(22)

$$F=\frac{4\left(L_a-L_u^{tip}\right)mf_r}{\left(\theta_2-\theta_1\right)L_u^{tip}\left(L_u^{tip}-mf_r\right)^2}\left[\left(L_u^{tip}-mf_r\right)\left(\frac{\pi}{P_r}-\theta_2\right)-f_rL_u^{tip}\ln\left(\frac{L_u^{tip}\left(\frac{\pi}{P_r}-\theta_2-f_r\right)-mf_r\left(\frac{\pi}{P_r}-\theta_2\right)}{f_rL_u^{tip}}\right)\right]$$
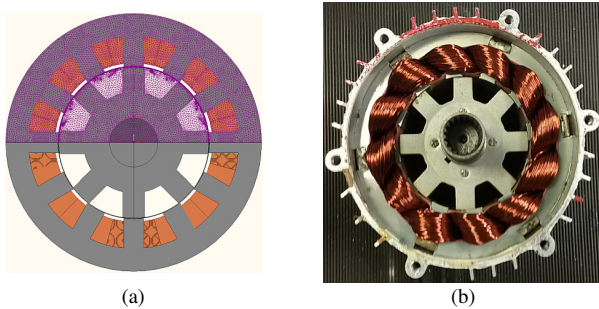
(23)

(a)           (b)

Fig. 10. Cross sectional views of the FEA model (a) and physical prototype (b).

## A. Trapezoidal Inductance Profile

The trapezoidal inductance profile is evaluated as discussed in Section III. Experimental inductances have been measured by an N4L-PSM1735-IAI impedance analyser, with the rotor being locked at every 1.25° (mech.).

To construct the pseudo-trapezoidal analytical locus, the experimental value of the aligned inductance $L_a$ has been considered for the full-overlap region. For the partial-overlap region, the gradient $s$ has been evaluated by substituting the measured $L_a$ and $L_u^{tip}$ into (5). $\theta_1$ and $\theta_2$ are 0.939°(mech.) and 16.16°(mech.) respectively. Then, the experimental values of $L_u^{tip}$ and $L_u$ have been fitted into the Fröhlich-like curve presented in Section III The analytical profile is compared against those obtained by FEA and experimentally, in Fig. 11. The key inductances of the three profiles are compared in Table II. A good match over the whole range of rotor positions is observed, with excellent similarity achieved for the non-overlapping region.

TABLE II
Analytical, FE and experimental inductance values of the SR prototype

|  | $L_a$ (mH) | $L_u^{tip}$ (mH) | $L_u$ (mH) |
|---|---|---|---|
| **Analytical** | 1.540 | 0.441 | 0.275 |
| **FE** | 1.531 | 0.399 | 0.272 |
| **Experimental** | 1.540 | 0.441 | 0.275 |

## B. Variable Advance Angle Testing

In this Subsection, the closed-form expression of $\theta_{ad}^*$ given in (18) is validated against the torque vs. advance
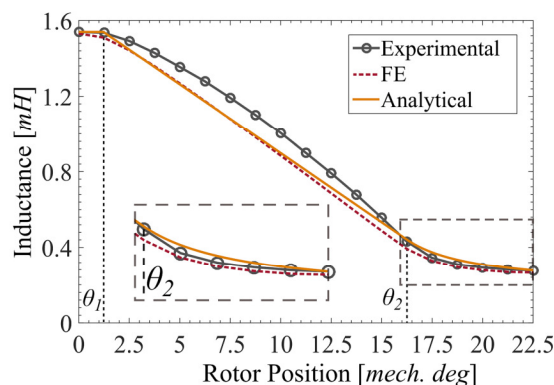


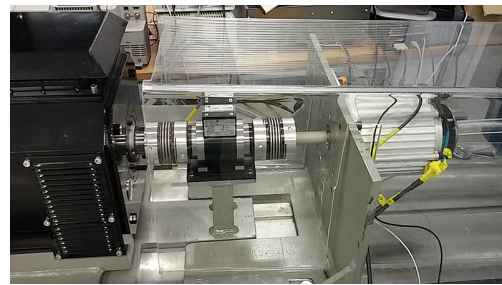Fig. 11. Inductance vs. Rotor Position characteristics of the prototype SR machine.



Fig. 12. SR prototype under test coupled to a high-speed IM in the test rig.

angle profile obtained from a full set of FEA simulations and from the experimental data. The experimental validation has been conducted on a fully instrumented test rig (Fig. 12), with the prototype SR machine coupled to a high-speed induction machine. Four sets of tests have been considered with the following combinations of dc-bus voltage and rotating speed: 1) 24V, 5000rpm, 2) 24V, 6000rpm, 3) 36V, 5000rpm and 4) 36V, 6000rpm.

The results are plotted in Fig. 13 (a) and (b). The optimal advance angle $\theta_{ad}^*$ determined by (18) is found to be 111.49°(elec.). Plots in Fig. 13 demonstrate that such a value closely matches with the torque-maximising angles of both the FEA and experimental profiles.

In Table III, the value of $\theta_{ad}^*$ determined by (18) is compared against the torque-maximising angles estimated via FEA $\theta_{ad\_FE}^*$, at the four operating conditions at hand. As it can be noted, discrepancies oscillate between the 3% and the 6%. In particular, results show that such discrepancy is slightly higher at the lower speed. This is due to the resistive voltage drop effect, which decreases as the speed increases.

Table IV compares the torque obtained with the single-shot FEA simulation using $\theta_{ad}^*$, i.e. $T(\theta_{ad}^*)$, against the maximum torque obtained from the FEA profile $T_{MAX\_FE}$. Results show that discrepancies are well below 1%.

By comparing results of Tables III and IV, it is observed that the errors incurred in the optimal angle estimation marginally affect the evaluated maximum torque.

## VI. MAXIMUM-SPEED-NODE DESIGN: A CRITICAL ANALYSIS

In this Section, a deeper insight into design at the maximum-speed node follows from the model developed in Sections III and IV and the results' validation of Section V. Firstly, the accuracy in the maximum torque evaluation is tested for different SR machines, with $\theta_{ad}^*$ found via (18) and FEA torque computation. Secondly, the improvement in computation time achieved by introducing (18) in a design routine is shown. Thirdly, the possibility to calculate analytically even the maximum torque is analysed. Finally, the possibility to change the control angles to improve other performance is briefly discussed.

TABLE III
Optimal Advance Angles Computed Analytically, $\theta_{ad}^*$, and by FE, $\theta_{ad\_FE}^*$

|  | $\theta_{ad}^*$ [°electrical] | $\theta_{ad\_FE}^*$ [°electrical] | DISCREPANCY $\Delta\theta_{ad}^*$ [%] |
|---|---|---|---|
| **24V, 5000rpm** | 111.49 | 104.88 | +6.30 |
| **24V, 6000rpm** | 111.49 | 107.92 | +3.3 |
| **36V, 5000rpm** | 111.49 | 104.88 | +6.30 |
| **36V, 6000rpm** | 111.49 | 107.92 | +3.3 |

TABLE IV
FEA-computed maximum Torque found for $\theta_{ad}^*$ and $\theta_{ad\_FE}^*$

|  | $T(\theta_{ad}^*)$ [Nm] | $T_{MAX\_FE}$ [Nm] | DISCREPANCY $\Delta T$ [%] |
|---|---|---|---|
| **24V, 5000rpm** | 0.981 | 0.984 | -0.30 |
| **24V, 6000rpm** | 0.696 | 0.698 | -0.28 |
| **36V, 5000rpm** | 2.206 | 2.214 | -0.36 |
| **36V, 6000rpm** | 1.565 | 1.569 | -0.25 |

## A. Maximum Torque Error Analysis

The robustness of (18) is now demonstrated by analysing the error in the maximum torque for SR machines having different geometries and operating conditions. To this end, six SR machines, different from the above prototype, have been modelled via FEA. Their main parameters are described in Table V, where $P_s$ and $P_r$ indicate the number
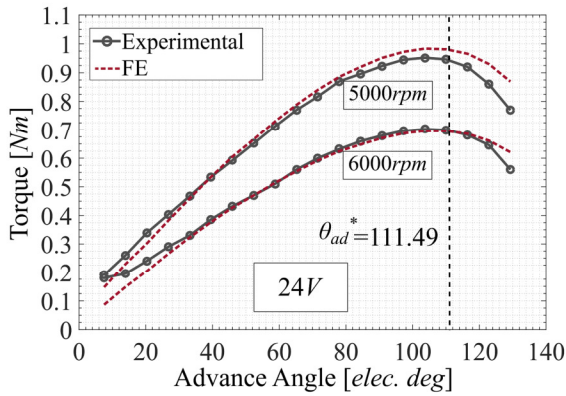


(a)
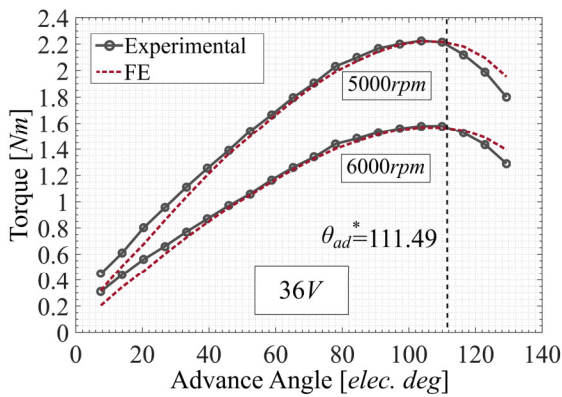


(b)

Fig. 13. FEA and experimental output torque vs. advance angle, characteristics at: (a) 24V, 5000rpm and 6000rpm; (b) 36V, 5000rpm and 6000rpm.

TABLE V
FEA-modelled SR machines: maximum torque error analysis

|  | $P_s/P_r$ | $V_{DC}$ [V] | $\omega_{MAX}$ [rpm] | $\theta_{ad}^*$ [°elec.] | $\Delta\theta_{ad}^*$ [%] | $T(\theta_{ad}^*)$ [Nm] | $\Delta T$ [%] |
|---|---|---|---|---|---|---|---|
| **SR_A** | 6/4 | 90 | 35000 | 129.25 | 0.98 | 6,40 | -0,08 |
| **SR_B** | 6/4 | 90 | 15000 | 120.17 | 1,84 | 4,43 | -0,09 |
| **SR_C** | 12/8 | 240 | 12000 | 124.39 | 10,1 | 55,7 | -3,07 |
| **SR_C** (linear iron) | 12/8 | 240 | 12000 | 120.17 | 1,13 | 43,4 | -0,03 |
| **SR_D** | 12/8 | 120 | 9000 | 128.7 | -0,23 | 27,1 | -0,22 |
| **SR_E** | 16/14 | 500 | 12000 | 109.1 | 1,02 | 11,8 | -0,02 |

of stator and rotor poles respectively, $\Delta\theta_{ad}^*$ and $\Delta T$ are the discrepancies defined in Table III and Table IV. The analysis confirms that the accuracy in the maximum-torque calculation is marginally affected from the error in the advance angle. This is due to the flat-topped shape of the torque vs. $\theta_{ad}$ characteristics, which can be seen in Fig. 13. From the analysis, it is possible to highlight the potential causes of the error $\Delta\theta_{ad}^*$:

1. Non-negligible resistive voltage drop, as seen in Section V;
2. Discrepancy between the analytical and the real inductance profiles;
3. Non-negligible local saturation effects.

In regard of point 3 above, machine SR_C, which is rated for 65kW and 300Arms, provides a good example to show the effects of local saturation. Fig. 14 shows SR_C's flux density distribution with the 400A phase current absorbed at the turn-off instant, which represents the perceived worst-case condition. Here, local saturation is present in the overlapping area, whereas the rest of the stator tooth remains below the saturation level. In order to gain a better insight into this phenomenon, SR_C has been modelled also with an ideal iron ($10^6 H/m$ permeability). As shown in Table V, if the saturation effects are removed, the error in the advance angle estimation drops from the 10% to the 1% and consequently the error in the maximum torque drops from 3% to 0%. In any case, due to the error mitigation discussed above, the 3% error of the 'real' machine is perfectly acceptable for design purposes. On the other hand, the 10% error in the optimal angle estimation highlights that
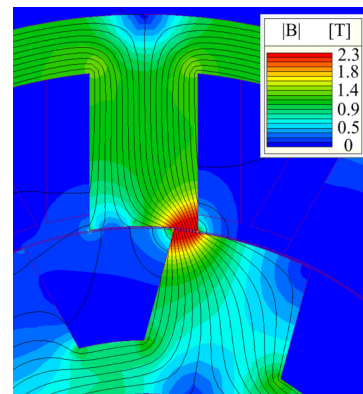


Fig. 14. SR_C flux density distribution at the turn-off instant with a 400A phase current.

when local saturation effects are not entirely negligible, a non-negligible error in the estimation of $\theta_{ad}^*$ might occur. Therefore, in case $\theta_{ad}^*$ itself is being searched, e.g. for a controller development, the result of (18) might have to be verified with an accurate iterative algorithm. However, it is possible to observe that:

1. Such a limitation does not affect the design process, since control system development is carried out only after the design has been completed;
2. Even in this case, (18) may result of great help, since it can provide an educated guess for the initial value of the iterative algorithm, which accelerates its convergence.

### B. Improvement in Computational Time

In this Subsection, a benchmark maximum-speed-node design is considered. The objective is to show the reduction in computational time that is achieved when (18) replaces the FEA-based optimisation algorithm to find the maximum torque. The case study is the design of the same SR machine used in Section V. A 1.48$Nm$ torque is required at 6000$rpm$ (1.25$HP$). The design process is based on the selection of the best candidate from a population of 1250 candidates. For every machine candidate, the maximum torque available at 6000$rpm$ is found using two different methods:

o Method 1: $\theta_{ad}^*$ is evaluated directly from (18) and fed into the one-shot FEA simulation.

o Method 2: the torque vs. advance angle locus is built up with a FEA-based search-grid algorithm, [27]. Firstly, in the interval of $\theta_{ad}$ between 60° and 160°, a 6-node coarse grid is created. The corresponding torques are computed and the first-iteration torque-maximising advance angle $^1\theta_{ad}$ is kept. Subsequently, a finer 9-node grid is created around $^1\theta_{ad}$. Then, the corresponding torques are computed and the maximum one is finally taken as maximum torque.

The routine is implemented in MATLAB and runs on a workstation, with an i7-3630 processor @2.40 GHz, 24 GB RAM. The computation times of the two methods are compared in Table VI. As expected, Method 1 is 14.45 times faster than Method 2, since the latter requires the evaluation of the output torque fifteen times for every machine candidate.

TABLE VI
Comparison of computation times to evaluate the maximum torque at 6000rpm. Method 1 vs. Method 2

| | Computation time for 1250 candidates [hours] |
|---|---|
| Method 1 | 2.5 |
| Method 2 | 36.4 |

### C. Possibility of Maximum Torque Analytical Calculation

In the previous parts of this work, the analytical process interrupts at the evaluation of $\theta_{ad}^*$ by means of (18). Then,

$\theta_{ad}^*$ is fed into a one-shot FEA simulation to get the maximum torque. This Subsection discusses the possibility of making the entire process analytical, by feeding $\theta_{ad}^*$ directly into (15) to calculate the maximum torque $T_{ANA}(\theta_{ad}^*)$. In Fig. 15, for the SR prototype running at 5000$rpm$, 36$V$, the $T_{avg}$ vs. $\theta_{ad}$ locus is compared against the experimental and FEA loci of Fig. 13(b). $T_{ANA}(\theta_{ad}^*)$ is compared against $T_{max\_FE}$ in Table VII. Data show a 6.46% discrepancy $\Delta T_{\_ANA}$, which is much more significant than the -0.36% incurred with an FEA torque evaluation.

Considering an entire design process, such a relatively low accuracy may be acceptable for the very early stages, i.e. initial sizing or trade-off studies. Hence, for this kind of tasks, a fully-analytical process can be taken into account. However, for the largest part of the design process, a much higher accuracy is required and therefore FEA torque evaluation becomes necessary. All the above explains the reason why, in this work, torque computation via FEA has been proposed as main option.

TABLE VII
SR prototype: Analytically-computed vs. FEA-computed maximum Torque

| | $T_{MAX\_ANA}$ [$Nm$] | $T_{MAX\_FE}$ [$Nm$] | DISCREPANCY $\Delta T_{ANA}$ [%] |
|---|---|---|---|
| 24V, 5000rpm | 2.357 | 2.214 | 6.46 |

### D. Considerations about changing the control angles to meet other Performance at the Maximum-Speed Node

This Subsection analyses the possibility to change the control angles to improve other performance during the design at the maximum-speed node, e.g. losses and efficiency.

As it has been explained in Section II, the first task is to verify that the maximum power available $P_{max}(\omega_{max})$ is at least equal to the rated power $P_{rated}$. To this end, the maximum available dc-bus voltage is taken, $\Theta_{dwell}$ is set to 180°(elec.) and the torque-maximising $\theta_{ad}$ is found. For convenience, the quantity $\Delta P$ is introduced:
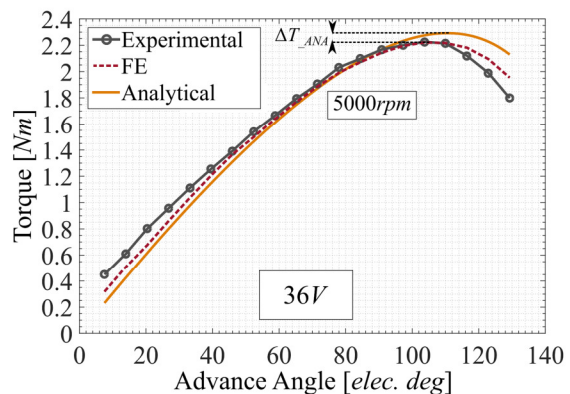


Fig. 15. Output torque vs. advance angle, characteristics at 6000$rpm$, 36$V$: Experimental, FE and Analytical results.

$$\Delta P = P_{\max}(\omega_{\max}) - P_{rated}. \tag{24}$$

The possibility to change the control angles depends on the value of $\Delta P$, for whose evaluation (18) is still necessary. Three possible scenarios exist.

In the first, $\Delta P$ is negative, meaning that the design candidate under consideration cannot meet the power requirement and hence must be discarded.

In the second case, $\Delta P$ is equal or slightly greater than zero, meaning that the design candidate at hand meets the power requirement. On the other hand, the control angles have been already fixed, such that there are no degrees of freedom left to optimise other performance. However, for wide-CPSR applications, SR machines designs with $\Delta P$ almost equal to zero are relatively common, [3], [22]. In fact, development of the rated power up to the maximum speed is normally very challenging. Besides, even under maximum-torque operation, performance remain in the typical range. For example, losses and efficiency of the SR prototype considered above, found via FEA, are reported in Table VIII. A 90% efficiency value, typical of SR machines running in single-pulse mode can be observed.

Finally, the case with $\Delta P$ significantly greater than zero is possible as well. In this situation, the designer has enough degrees of freedom to change the control angles. Thus, it is possible to operate the SR machine at a power level that is lower than the maximum, in return for the optimisation of one (or more) further performance.

In particular, [15], [16], illustrate the FEA-based methodology to set $\theta_{ad}$ and $\Theta_{dwell}$ to maximise the efficiency for a given rated power. In this condition, the most convenient strategy is to keep $\theta_{ad}$ constant and reduce $\Theta_{dwell}$. In [28], other examples of control strategies aimed at different performance optimisation in high-speed, single-pulse mode are provided. Significant differences with the low-speed chopping mode operation can be observed, [29].

In conclusion, in order to be able to change the control angles, an oversized machine design must be accepted.

TABLE VIII
Losses and Efficiency of the SR prototype at 36$V$, 5000$rpm$ and 6000$rpm$

|  | COPPER LOSSES [W] | IRON LOSSES [W] | EFFICIENCY [%] |
|---|---|---|---|
| 36$V$, 5000$rpm$ | 116.59 | 17.12 | 90.02 |
| 36$V$, 6000$rpm$ | 81.77 | 15.44 | 91.32 |

## VII. CONCLUSION

In this paper, an analytical closed-form expression that identifies the torque-maximising advance angle of an SR machine at high-speed, single-pulse mode conditions has been proposed, with the intention to aid the design at the maximum-speed node. Such closed-form expression has been validated on an SR prototype and on six SR machines modelled through FEA. The main outcome of this work is that the proposed closed-form expression is a key 'tool in the box' for the design at the maximum-speed node, since:

- It allows to significantly reduce the design computation time, as the maximum output torque is found via a single-shot FEA simulation, without any need for iterative optimisation algorithms;
- An insignificant loss of accuracy for the maximum output torque estimation is found. For example, the error resulted lower than the 1% for the SR prototype and lower than the 3% in the worst case of the FEA-modelled SR machines.

## VIII. REFERENCES

[1] J. B. Bartolo, M. Degano, J. Espina, and C. Gerada, "Design and Initial Testing of a High-Speed 45-kW Switched Reluctance Drive for Aerospace Application," *IEEE Transactions on Industrial Electronics,* vol. 64, no. 2, pp. 988-997, 2017.

[2] H. Zhang, W. Xu, S. Wang, Y. Huangfu, G. Wang, and J. Zhu, "Optimum Design of Rotor for High-Speed Switched Reluctance Motor Using Level Set Method," *IEEE Transactions on Magnetics,* vol. 50, no. 2, pp. 765-768, 2014.

[3] P. Moreno-Torres, M. Lafoz, M. Blanco, G. Navarro, J. Torres, and L. García-Tabarés, "Switched Reluctance Drives with Degraded Mode for Electric Vehicles," *Modeling and Simulation for Electric Vehicle Applications,* pp. 97-124, 2016.

[4] J. W. Jiang, B. Bilgin, and A. Emadi, "Three-Phase 24/16 Switched Reluctance Machine for a Hybrid Electric Powertrain," *IEEE Transactions on Transportation Electrification,* vol. 3, no. 1, pp. 76-85, 2017.

[5] K. Kiyota and A. Chiba, "Design of Switched Reluctance Motor Competitive to 60-kW IPMSM in Third-Generation Hybrid Electric Vehicle," *IEEE Transactions on Industry Applications,* vol. 48, no. 6, pp. 2303-2309, 2012.

[6] V. Madonna, P. Giangrande, and M. Galea, "Electrical Power Generation in Aircraft: Review, Challenges, and Opportunities," *IEEE Transactions on Transportation Electrification,* vol. 4, no. 3, pp. 646-659, 2018.

[7] K. M. Rahman and M. Ehsani, "Performance analysis of electric motor drives for electric and hybrid electric vehicle applications," in *Power Electronics in Transportation*, 1996, pp. 49-56.

[8] M. A. Kabir and I. Husain, "Design of Mutually Coupled Switched Reluctance Motors (MCSRMs) for Extended Speed Applications Using 3-Phase Standard Inverters," *IEEE Transactions on Energy Conversion,* vol. 31, no. 2, pp. 436-445, 2016.

[9] T. J. E. Miller, *Switched Reluctance Motors and their Control* (Monographs in Electrical and Electronic Engineering). Oxford: Oxford University Press, 1993.

[10] J. Faiz and J. W. Finch, "Aspects of design optimisation for switched reluctance motors," *IEEE Transactions on Energy Conversion,* vol. 8, no. 4, pp. 704-713, 1993.

[11] A. V. Radun, "Design considerations for the switched reluctance motor," *IEEE Transactions on Industry Applications,* vol. 31, no. 5, pp. 1079-1087, 1995.

[12] C. Ma and L. Qu, "Multiobjective Optimization of Switched Reluctance Motors Based on Design of Experiments and Particle Swarm Optimization," *IEEE Transactions on Energy Conversion,* vol. 30, no. 3, pp. 1144-1153, 2015.

[13] R. Rocca, F. Giulii Capponi, G. De Donato, M. Rashed, S. Papadopoulos, and M. Galea, "Analytical Approach for the Identification of an Optimal Design Space for Switched Reluctance Machines," in *2018 XIII International Conference on Electrical Machines (ICEM)*, 2018, pp. 569-575.

[14] T. J. E. Miller, *Switched Reluctance Motors and their Control* (Monographs in Electrical and Electronic Engineering). Oxford, 1993.

[15] W. Shiliang, Y. Zhuo, and G. Lei, "Core loss analysis for switched reluctance motor under hysteresis current control and single pulse modes," in *2016 IEEE Transportation Electrification Conference and Expo (ITEC)*, 2016, pp. 1-6.

[16] J. Kim and R. Krishnan, "High Efficiency Single-Pulse Controlled Switched Reluctance Motor Drive for High Speed (48k RPM)

Application: Analysis, Design, and Experimental Verification," in *2008 IEEE Industry Applications Society Annual Meeting*, 2008, pp. 1-8.

[17] H. Hannoun, M. Hilairet, and C. Marchand, "Design of an SRM Speed Control Strategy for a Wide Range of Operating Speeds," *IEEE Transactions on Industrial Electronics,* vol. 57, no. 9, pp. 2911-2921, 2010.

[18] M. Rekik, M. Besbes, C. Marchand, B. Multon, S. Loudot, and D. Lhotellier, "High-speed-range enhancement of switched reluctance motor with continuous mode for automotive applications," *European Transactions on Electrical Power,* vol. 18, pp. 674-693, 2008.

[19] H. Hannoun, M. Hilairet, and C. Marchand, "Experimental Validation of a Switched Reluctance Machine Operating in Continuous-Conduction Mode," *IEEE Transactions on Vehicular Technology,* vol. 60, no. 4, pp. 1453-1460, 2011.

[20] M. Lipták, "Principle of Design of Four Phase Low Power Switched Reluctance Machine Aimed to the Maximum Torque Production," *Journal of ELECTRICAL ENGINEERING,* vol. 55, no. 5-6, pp. 138-143, 2004.

[21] M. Moallem and C. M. Ong, "Predicting the steady-state performance of a switched reluctance machine," *IEEE Transactions on Industry Applications,* vol. 27, no. 6, pp. 1087-1097, 1991.

[22] S. Roggia, Y. C. Chong, Y. Gai, M. Popescu, D. Staton, and J. Goss, "Switched Reluctance Machine Peak and Continuous Performance Using a Routine Optimised Tool," in *2019 IEEE International Electric Machines & Drives Conference (IEMDC)*, 2019, pp. 584-590.

[23] S. Vukosavic and V. R. Stefanovic, "SRM inverter topologies: a comparative evaluation," *IEEE Transactions on Industry Applications,* vol. 27, no. 6, pp. 1034-1047, 1991.

[24] M. Rekik, M. Besbes, C. Marchand, B. Multon, S. Loudot, and D. Lhotellier, "Improvement in the field-weakening performance of switched reluctance machine with continuous mode," *IET Electr. Power Appl,* vol. 1, no. 5, pp. 785–792, 2007.

[25] R. Krishnan, *Switched reluctance motor drives: modeling, simulation, analysis, design, and applications* (Industrial Electronics Series). Florida: CRC Press LLC, 2001.

[26] T. J. E. Miller and M. McGilp, "Nonlinear theory of the switched reluctance motor for rapid computer-aided design," *IEE Proceedings B - Electric Power Applications,* vol. 137, no. 6, pp. 337-347, 1990.

[27] C.-w. Hsu, C.-c. Chang, and C.-J. Lin, *A Practical Guide to Support Vector Classification*. 2003.

[28] J. W. Jiang, F. Peng, B. Bilgin, and A. Emadi, "Optimisation-based procedure for characterising switched reluctance motors," *IET Electric Power Applications,* vol. 11, no. 8, pp. 1366-1375, 2017.

[29] X. D. Xue *et al.*, "Optimal Control Method of Motoring Operation for SRM Drives in Electric Vehicles," *IEEE Transactions on Vehicular Technology,* vol. 59, no. 3, pp. 1191-1204, 2010.

## IX. Biographies
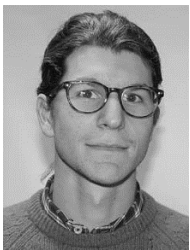
**Roberto Rocca** (S'15) received the M.S. [Hons.] in electrical engineering from the University of Rome "La Sapienza," Rome, Italy, in 2015. From 2015 he is pursuing the Ph.D. degree with the Power Electronics, Machines and Control (PEMC) Group at the University of Nottingham, Nottingham, UK. From 2019, he is also serving as Research Associate at the Department of Astronautical, Electrical, and Energy Engineering of the University of Rome "La Sapienza," Rome, Italy. He is Member of the IEEE Industry Applications and the IEEE Power and Energy Societies. His main research interests revolve around the multiphysics design and analysis of electrical machines and drives, analytical and numerical modelling of electromechanical devices and innovative electric energy storage systems

**Fabio Giulii Capponi** (M'98) received the M.S. and Ph.D. degrees in electrical engineering from the University of Rome "La Sapienza," Rome, Italy, in 1994 and 1998, respectively. From 1996 to 2015, he was an Assistant Professor with the University of Rome "La Sapienza," where he is currently an Associate Professor of Electrical Machines, Converters, and Drives in the Department of Astronautical, Electrical, and Energy Engineering. In 2003 and 2004, he was a Visiting Scholar at the Wisconsin Electrical Machines and Power Electronics Consortium (WEMPEC), University of Wisconsin, Madison, WI, USA. He is author or co-author of more than 90 published technical papers. His current research interests include permanent magnet motor drives and multi-physics design of electrical machines. Prof. Giulii Capponi is a Registered Professional Engineer in Italy and is Member of the IEEE Industry Applications, the IEEE Industrial Electronics, and the IEEE Power Electronics Societies. He is a Member of the IEEE IAS Industrial Drives Committee, the Electric Machines Committee, and the Transportation Systems Committee. He received the 2014 First Prize Paper Award and the 2016 Third Prize Paper Award, both from the IAS Industrial Drives Committee.

**Savvas Papadopoulos** completed his PhD degree in the Power Electronics, Machines and Control Group (PEMC) of the University of Nottingham in 2016 where he also continued to work as a research fellow. In 2019, he has been appointed as lecturer in electrical engineering at Edinburgh Napier University. His research interests relate power electronics converter design and their role in the electrification of transport.

**Giulio De Donato** (S'05–M'08–SM'17) received the M.S. and Ph.D. degrees in electrical engineering from the University of Rome "La Sapienza," Rome, Italy, in 2003 and 2007, respectively. From 2007 to 2008, he was a Research Associate with the Department of Electrical Engineering, University of Rome "La Sapienza," where, from 2008 to 2010, he was an Assistant Professor, and since 2010, he has held the same position with the Department of Astronautical, Electrical, and Energy Engineering (DIAEE). Since 2019, he is an Associate Professor with the same department. He is co-PI of a collaborative research agreement between the DIAEE and the Department of Electrical, Electronic Engineering, and Computer Science, University of Catania, for research in the field of wide-bandgap semiconductor-based drives. His current research interests include digital control of brushless drives, analysis and design of permanent-magnet machines, and wide-bandgap-semiconductor-based power converters. G. De Donato is a Member of the IEEE Industry Applications, the IEEE Industrial Electronics, and the IEEE Power Electronics Societies. He is a Member of the IEEE IAS Industrial Drives Committee, the IAS Electric Machines Committee, the IES Electrical Machines Committee, and the PELS Technical Committee on Motor Drives and Actuators. He was the recipient of the 2014 First Prize Paper Award and the 2016 Third Prize Paper Award, both from the IAS Industrial Drives Committee. He is currently an Associate Editor for the IEEE Transactions on Industry Applications.

This article has been accepted for publication in a future issue of this journal, but has not been fully edited. Content may change prior to final publication. Citation information: DOI 10.1109/TEC.2019.2959823, IEEE Transactions on Energy Conversion

12

**Mohamed Rashed** (M'07) received the Ph.D. degree in electrical motor drives from the University of Aberdeen, Aberdeen, U.K., in 2002. He was a Post-Doctoral Research Fellow with the Department of Engineering, University of Aberdeen for the periods, from 2002 to 2005 and from 2007 to 2009. In 2005, he was appointed as an Assistant Professor with the Department of Electrical Engineering, Mansoura University, Mansoura, Egypt, and then on leave from 2007. In 2008, he was promoted to Associate Professor in Mansoura University, Egypt. Since 2009, he is with the Power Electronics, Machines and Control (PEMC) Research Group, Department of Electrical and Electronic Engineering, The University of Nottingham, Nottingham, U.K., where he is currently a Senior Research Fellow. His current research interests include the design and control of electrical motor drives and power systems for aerospace applications, power electronics for micro grids, renewable energy sources, and energy storage systems.

**Michael Galea** (SM'18) received the Ph.D. degree in electrical machines design in 2013 from the University of Nottingham, Nottingham, U.K. He was appointed as Lecturer in 2014, as Associate Professor in 2018 and as Professor in Electrical Machines and Drives in 2019, all with the University of Nottingham. He is currently the Head of School of Aerospace, University of Nottingham Ningbo China, where he is also the Director of Aerospace. He currently lectures in Electrical Machines and Drives and in Aerospace Systems Integration and manages a number of diverse projects and programs related to the more/all electric aircraft, electrified propulsion, and associated fields. His main research interests include design and development of electrical machines and drives (classical and unconventional), reliability and lifetime degradation of electrical machines and the more electric aircraft. Michael is a Fellow of the Royal Aeronautical Society, a Senior Member of the IEEE and sits on the Executive Board of the UK Magnetics Society.